# A Compact Harmonic Radar System With Active Tags at 61/122 GHz ISM Band in SiGe BiCMOS for Precise Localization

Steffen Hansen, *Graduate Student Member, IEEE*, Christian Bredendiek, *Member, IEEE*, Gunnar Briese, and Nils Pohl, *Senior Member, IEEE*

***Abstract*— This article presents a frequency-modulated continuous wave (FMCW) harmonic radar in the 61-/122-GHz industrial, scientific, and medical (ISM) frequency bands. The radar is based on two self-designed monolithic microwave wave integrated circuits (MMICs) for the transceiver (TRX) and tag which are fabricated in a 130-nm SiGe BiCMOS technology. The presented TRX-MMIC consists of a fundamental voltage-controlled oscillator (VCO), a power amplifier (PA), Wilkinson power dividers, and a static divide-by-16 chain for stabilization within a phase-locked loop (PLL) in the transmitter (TX) part. The receiver (RX) part has two channels with a low noise amplifier (LNA), a Gilbert cell mixer, and an intermediate frequency (IF)-amplifier each. The fundamental of the VCO is converted by a frequency doubler and distributed to the local oscillator (LO) input of the RX-mixers. With such a TRX architecture the active nonlinear tag which consists of antennas, pre-amplifiers, and a frequency doubler can be detected. For a sweep from 60 to 64 GHz, a spatial resolution of 4 cm at 1-m distance and a range of 23.3 m is achieved. With these characteristics, the tag enables harmonic radar applications in the millimeter-wave (mm-wave) range for medium range with high accuracy and resolution with a small form factor.**

***Index Terms*— Backscatter, clutter suppression, *D*-band, frequency-modulated continuous wave (FMCW), frequency doubler, harmonic, industrial, scientific, and medical (ISM), millimeter-wave (mm-wave), monolithic microwave wave integrated circuit (MMIC), radar, radio frequency identification (RFID), secondary radar, SiGe, tag, *V*-band.**

## I. Introduction

UNIQUELY identifying the intended target can be a challenging task for conventional frequency-modulated continuous wave (FMCW) radar in an environment with heavy clutter. Although FMCW radar sensors can achieve accuracies in the $\mu$m-range [1] for a clean and strong response of the target, the performance metrics are limited for complex sceneries. Especially when the radar cross section (RCS) is small, the signal-to-interference ratio (SIR) and thus the accuracy can become small. In the worst case, the target of interest cannot be detected at all. These challenges can be met by applying a harmonic reflector, the tag, on the target of interest. The tag which consists of antennas and a nonlinear device has a response at a harmonic frequency that is distinguishable from the background which is mostly linear. With a receiver also at the corresponding harmonic frequency, only the response of the tag is converted to the intermediate frequency (IF) and the clutter is not detected.

In the literature, many different harmonic radar systems are presented (see Table I). In most applications, compact and passive tags are attached to insects or other animals with a small RCS the nonlinear tag is distinguishable from the clutter of foliage. These systems are mostly designed below the millimeter-wave (mm-wave) frequency range where higher output power and lower free-space path loss (FSPL) are achievable. While some systems [5], [6] achieve high detection ranges above 100 m they rely on fairly high output power and big focusing antennas at the TRX, thus the systems need to be installed at place. There are also some systems [2]–[4] presented that are designed for lower range and portable use. However, below the mm-waves, the systems are still quite heavy and not suitable for industrial applications. Toward higher frequencies, a conversion at passive tags becomes increasingly inefficient as shown in [9] where a 38.5-/77-GHz harmonic radar in the mm-waveband is presented. Here, a Schottky diode is biased by a photodiode for lower conversion loss to extend the detection range to 1 m. In [10], nonlinear reflectors for integration into the clothing of vulnerable road users (VRUs) in the 77-GHz-automotive band are presented. Instead of receiving at twice the fundamental frequency, they transmit two waveforms with a small offset and receive the 3rd order inter-modulation product which is close to the fundamental frequency. With this concept, only one antenna for TX and RX, respectively, is needed but the system does not benefit from the increased bandwidth resulting from frequency translation to the harmonic frequency. With the high equivalent isotropic radiated power (EIRP) $P_{\mathrm{EIRP}}$ allowed by the European Telecommunications Standards Institute (ETSI), a tag based on a high-Q micro-electro-mechanical

Manuscript received July 21, 2020; revised September 14, 2020; accepted September 15, 2020. Date of publication October 6, 2020; date of current version January 5, 2021. This work was supported in part by the "European Regional Development Fund" under Grant ERDF 2014-2020 and in part by the Ministry of Health, Equalities, Care and Aging of the State of North Rhine-Westphalia under Grant EFRE-0801729. *(Corresponding author: Steffen Hansen.)*

Steffen Hansen is with the Department of Integrated Circuits and Sensor Systems, Fraunhofer Institute for High Frequency Physics and Radar Techniques, 53343 Wachtberg, Germany (e-mail: steffen.hansen@fhr.fraunhofer.de).

Christian Bredendiek and Gunnar Briese are with Fraunhofer Institute for High Frequency Physics and Radar Techniques, 53343 Wachtberg, Germany.

Nils Pohl is with the Chair for Integrated Systems, Ruhr-University Bochum, 44801 Bochum, Germany.

Color versions of one or more of the figures in this article are available online at https://ieeexplore.ieee.org.

Digital Object Identifier 10.1109/TMTT.2020.3026353

TABLE I
COMPARISON OF STATE-OF-THE-ART HARMONIC RADAR SENSORS

| Ref, Year | Type | TX/RX - Freq. (GHz) | BW[#] (GHz) | $P_{\mathrm{TX}}$ (dBm) | Reader | | Tag | | Range (m) | Non-linear device |
|---|---|---|---|---|---|---|---|---|---|---|
| | | | | | $G_{\mathrm{TX,f}}$ (dBi) | $G_{\mathrm{RX,h}}$ (dBi) | $G_{\mathrm{TX,h}}$ (dBi) | $G_{\mathrm{RX,f}}$ (dBi) | | |
| [2], 2020 | FMCW | 2.9/5.8 | 0.16 | 34.7 | 13 | 14 | * | * | 40 | passive Schottky-Diode |
| [3], 2014 | LFM | 5.8/11.6 | 0.3 | 20 | 20 | 22 | 2 | 2 | 30 | passive Schottky-Diode |
| [4], 2008 | FMCW | 5.95/11.9 | 0.2 | 20 | 22 | 22 | 5.5 | 2.8 | 58 | passive Schottky-Diode |
| [2], 2020 | FMCW | 9.3/18.6 | 0.16 | 40 | 15 | 15 | * | * | 15 | passive Schottky-Diode |
| [5], 2019 | OOK | 9.4/18.8 | 0.022 | 60 | 26.6 | 27.3 | * | * | 500 | passive Schottky-Diode |
| [6], 2016 | PRN-code | 9.4/18.8 | 0.025 | 32.4 | 38 | 43 | -5 | -5 | 60 | passive Schottky-Diode |
| [7], 2016 | | | | | | | 0.2 | 0.2 | 180 | |
| [8], 2004 | pulsed | 9.41/18.82 | 0.001 | 66 | 15.8 | 24.5 | 2.41 | 1.64 | 200 | passive Schottky-Diode |
| [9], 2013 | CW | 38.5/77 | - | 21 | 25 | 24 | 6.73 | 6.71 | 1 | active[†] Schottky-Diode |
| [10], 2009 | | 77/77 | 2.5 | 15 | 40 | 40 | 16 | 16 | 22 | passive Schottky-Diode |
| | | | $10^{-7}$ | | | | | | 74[&] | passive MEMS Resonator |
| **[This]** | FMCW | 61/122 | 8 | 6 | 21 | 22.2 | 7.5 | 7.1 | 23 | active SiGe BiCMOS |

[#] Referred to the bandwidth of received signal which determines target accuracy and resolution.
* No information regarding the antenna gain is given. Here dipole-antennas are used which have in general a wide HPBW and low gain.
[†] The Schottky diode was here biased by a voltage supplied by a photodetector which was externally driven by a laser.
[&] The authors mention that due to the high Q-factor and the low bandwidth of the MEMS resonator in this very narrow band operation, the radar is not capable to detect the range of the reflector but only its direction and existence.

system (MEMS) resonator can be detected over 77-m distance and the distance to a tag based on Schottky diode can be measured to up to 22 m. The comparison in Table I shows that for this range the system additionally relies on relatively high gain antennas on TRX and tag.

Besides nonlinear reflectors, many publications on linear backscatterers to uniquely identifying the intended target by radio frequency identification (RFID) are presented in the literature. Passive tags are presented, for example, in the ultrahigh frequency (UHF) band in [11] to measure the filling-level in tanks but also in the mm-wave range at 76 GHz in [12] for automotive or in [13], where a passive RFID tag at 61 GHz with on-chip antennas was used to counter plagiarism. Even though the output power of the transponder is 17 dBm the range is only 23 mm because of the high FSPL and low on-chip antenna efficiency. Consequently, active tags are already developed for linear backscatterers with higher range in the mm-wave band. Especially the switched injection-locked oscillator (SILO) principle [14], [15] is capable of generating an approximately coherent output signal with high power for small input powers.

Recently, we published our first prototype of an active harmonic reflector tag based on a SiGe:C monolithic microwave wave integrated circuit (MMIC) for mm-wave harmonic radar applications [16]. We have shown that active tags can be a solution for the challenges of high FSPL and low output power, RX sensitivity, and conversion efficiency of passive tags. With the active tag, which adds sufficient gain to the power transfer equation in order to detect the target with a high signal-to-noise ratio (SNR) at medium distances, high absolute bandwidth for high range resolution and accuracy is achievable. In our recent publication, we presented measurements to characterize the conversion gain of the MMIC itself and the entire tag in a free space environment, respectively. The impulse response of the tag is measured by emulating the FMCW transceiver with a VNA. For a sweep of 2-GHz bandwidth, the tag shows a spatial resolution of 9.8 cm. This article is an extended version in which we present the earlier results of the harmonic reflector, which is a critical part of the system, for a proper explanation. Our latest results are added here. Especially the novelty of an integrated TRX (see Fig. 1) should be noted, which we use to carry out the free space measurements in this article. Such a compact transceiver and tag realizations as presented here can enable many applications for harmonic radar.

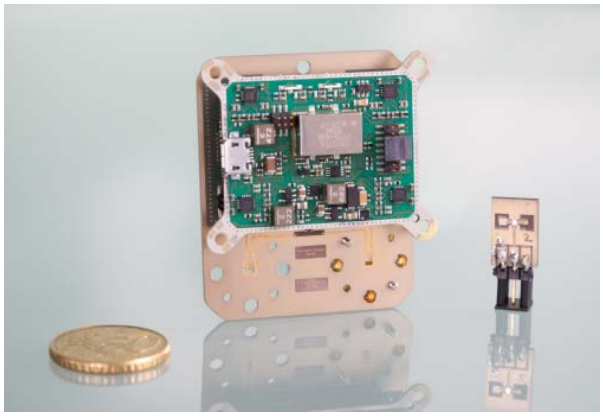

Fig. 1. Photograph of the harmonic radar TRX consisting of separate front-end and back-end to the left and tag to the right.

The following content of this article is organized in four parts. In Section II, the fundamentals and challenges of harmonic FMCW radar at mm-wave frequencies are described. Section III focuses on the design of the transceiver MMIC

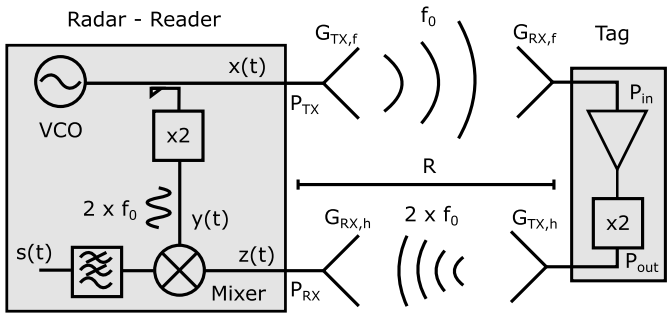


Fig. 2. Overview of the system and signal flow of the coherent harmonic FMCW radar.

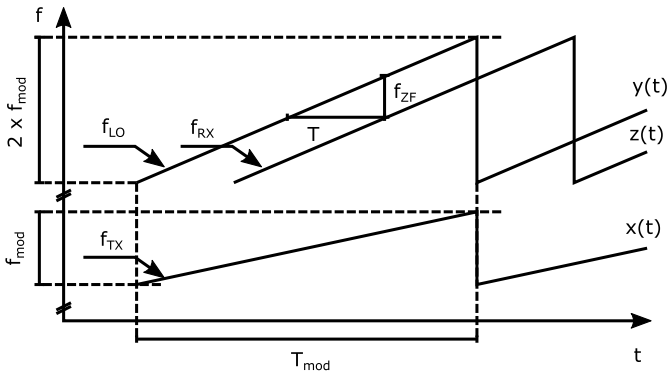


Fig. 3. Frequency ramps at TX, LO, and RX, respectively. Due to frequency multiplication, the bandwidth and slope are doubled at the receiving mixer.

(Section III-A) and front-end (Section III-B) as well as on the active tag (Section III-C). In Section IV measurement results with measurement equipment (Section IV-A) but also with the whole system (Section IV-B) are shown and in Section V conclusions are drawn.

## II. Harmonic Radar Fundamentals

### A. Basic Principle of Intermediate Frequency Generation

The harmonic radar is based on mixing a frequency unequal to the TX-frequency to the IF to suppress reflections from un-tagged targets. The tag which consists of antennas and a nonlinear device has a response at a harmonic frequency, which is distinguishable from the linear, passive environment. With a receiver also at the corresponding harmonic frequency, only the response of the tag is converted to the IF and the clutter can be suppressed when filtered out properly. In this article, a topology based on frequency doublers on the tag and the local oscillator (LO) path of the transceiver is chosen. They are used to mix the resulting coherent signal at the second harmonic as is presented in Fig. 2.

Consider Fig. 3 which shows a single frequency ramp of this approach. The voltage-controlled oscillator (VCO) is tuned over the bandwidth $f_{\mathrm{mod}}$ for the modulation duration $T_{\mathrm{mod}}$ and the signal with fundamental frequency $f_{\mathrm{TX}}$ is transmitted to the output $(x(t))$ or via the LO frequency doubler toward the RX mixer $(y(t))$. The tag is doubling the frequency of the signal transmitted by the TX-antenna which is then received at the RX-antenna of the TRX. The bandwidth and slope of

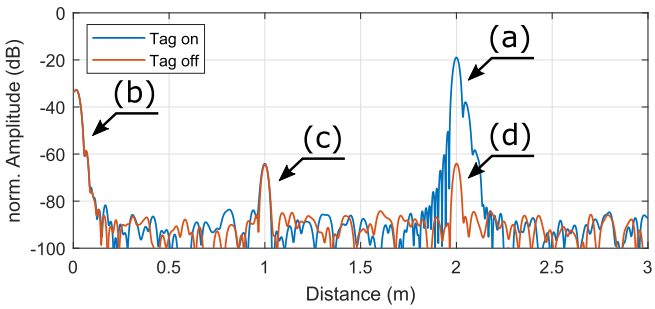


Fig. 4. Frequency-domain representation of simulated IF-signal of harmonic radar including interferers: (a) response of nonlinear active tag, (b) direct coupling from TX to RX, and clutter from reflections at the (c) fundamental and (d) harmonic frequency.

the ramp are doubled from the frequency translation as well. The resulting IF is proportional to the round trip time delay $\tau$ with

$$\tau = \frac{2R}{c} \tag{1}$$

$$f_{\mathrm{IF}} = \frac{2f_{\mathrm{mod}}}{T_{\mathrm{mod}}} \cdot \tau. \tag{2}$$

Noticeable is that in contrast to a conventional FMCW radar the bandwidth of the received signal is also doubled which accompanies with a better range resolution $\Delta R$ and accuracy $\sigma_R$

$$\Delta R \propto \frac{c}{4f_{\mathrm{mod}}} \tag{3}$$

$$\sigma_R = \frac{\Delta R}{\sqrt{2\mathrm{SNR}}}. \tag{4}$$

To achieve a clean IF-signal with high SIR, signal conditioning needs to be accounted. Consider Fig. 4 which shows a nonideal frequency-domain representation of a harmonic FMCW radar with a strong tag response at 2-m distance (a) and interference signals due to direct coupling (b) and a single linear reflector also at 2-m distance (c,d) which superimposes the carrier signal and are also present when the tag is switched off. Direct coupling (b) can occur between the antenna, the printed circuit board (PCB), or even on MMIC-level. In general, these interferences are easy to compensate as long as they do not saturate the receiver. They are of low frequency and reproducible since they depend on the traces on PCB and MMIC, respectively. Additionally, the distance to the tag is in most applications far enough away that for sufficient bandwidth the disturbing impulse can be separated from the carrier signal. The other group of interferers is a lot more complicated to handle since they depend on the distance of the wanted and unwanted targets, respectively. Sufficient suppression by filtering or isolation can handle these components. These are either mixing products at the fundamental frequency (c) which appear due to half the ramp slope at half their corresponding distance or at the second harmonic (d).

### B. Power Transfer Function

The nonlinear radar equation of a harmonic radar with active tags must be regarded separately for two cases. Either the input

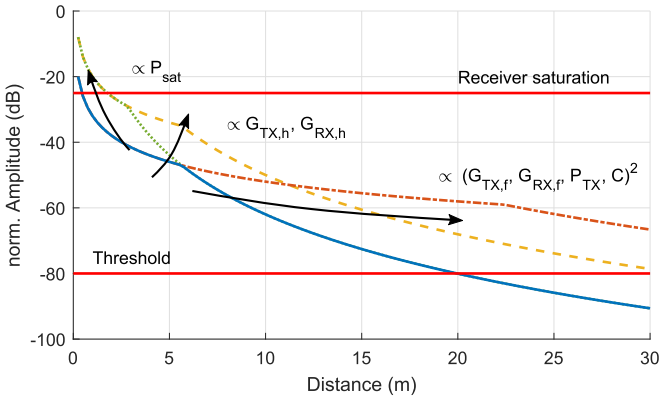


Fig. 5. Simulation of nonlinear Friis equation and dependence on system characteristics. Nonsolid curves result from increasing the sum of the corresponding parameters by 12 dB with respect to the blue solid line.

signal at the MMIC is above the input referred compression point $P_{\mathrm{I},-1\ \mathrm{dB}}$ and high enough to saturate the MMIC on the tag and the output power is equal to its saturated output power $P_{\mathrm{sat}}$ or otherwise, it is proportional to the square of the input power including a conversion gain factor C. For low input powers the frequency conversion becomes extremely inefficient

$$P_{\mathrm{out}} \approx \begin{cases} P_{\mathrm{sat}}, & P_{\mathrm{in}} \geq P_{\mathrm{I},-1\ \mathrm{dB}} \\ (P_{\mathrm{in}} C)^2, & \text{else.} \end{cases} \tag{5}$$

For the Friis transmission equation, this results in a term which is only dependent on the return path of the transmission link in particular $P_{\mathrm{sat}}$, the antenna gains at the harmonic frequency on transceiver $G_{\mathrm{RX},h}$ and tag $G_{\mathrm{TX},h}$ respectively and the wavelength at the harmonic frequency $\lambda_h$

$$P_{\mathrm{RX}} = P_{\mathrm{sat}} \cdot \frac{G_{\mathrm{TX},h} G_{\mathrm{RX},h} \lambda_h^2}{(4\pi R)^2.} \tag{6}$$

In this region, $P_{\mathrm{RX}}$ is proportional to $1/R^2$ as in a secondary radar. In the quadratic region, the entire transmission needs to be considered. Thus, instead of $P_{\mathrm{sat}}$ contributions prior to the MMIC, the output power of the transceiver $P_{\mathrm{TX}}$, the antenna gains at the fundamental frequency on transceiver $G_{\mathrm{TX},f}$ and tag $G_{\mathrm{RX},f}$ and C are included in the transmission equation

$$P_{\mathrm{RX}} = \left( \frac{P_{\mathrm{TX}} G_{\mathrm{TX},f} G_{\mathrm{RX},f} \lambda_f^2}{(4\pi R)^2} \cdot C \right)^2 \cdot \frac{G_{\mathrm{TX},h} G_{\mathrm{RX},h} \lambda_h^2}{(4\pi R)^2}. \tag{7}$$

Taking a closer look at the range and frequency dependence of this equation with $f = c_0/\lambda_f = c_0/2\lambda_h$ shows that the received power scales inverse proportionally to the sixth power of the distance and frequency in contrast to the fourth power of conventional radar

$$P_{\mathrm{RX}} \propto \left( \frac{1}{R \cdot f} \right)^6. \tag{8}$$

In Fig. 5, system simulations are given to show the dependencies on the remaining characteristics. The basis of this investigation is the solid blue curve which corresponds to system characteristics that are feasible at this frequency range. The influence of increasing the respective system characteristics are shown as nonsolid. One can separate these into three categories, depending on their influence on the power transfer function discussed earlier. A higher $P_{\mathrm{sat}}$ moves the transition between both regions toward lower distances. In general, this parameter has the least effect on the overall transmission equation. It needs to be high enough that the saturated region does not limit the range. On the other hand, it can be used to limit the signal power at the receiver in order to prevent receiver saturation. The increased gain $G_{\mathrm{TX},h}$ and $G_{\mathrm{RX},h}$ for the returning path transfer 1:1 into a higher signal amplitude. For high range measurements $G_{\mathrm{TX},f}$, $G_{\mathrm{RX},f}$, $P_{\mathrm{TX}}$, and C are most valuable since they contribute to the power of two but with those parameters increasing a high $P_{\mathrm{sat}}$ becomes increasingly important. Because of all these dependencies, the tag has to be designed for a specific application considering a trade-off between necessary angle and range of detection.

## III. System Design and Implementation

Consider Fig. 6 which shows a simplified block diagram of the harmonic FMCW radar in combination with a single active tag to provide an overview of the system. It consists of four main building blocks which are the MMIC, the front-end PCB, the back-end PCB of the reader, and the tag which is used as a radar target. Both TRX and tag are designed bistatic so that TX and RX on reader and tag can be designed for their respective frequency range which includes antenna- and matching network design. The downside of such a realization is that the antennas at the fundamental and harmonic frequency do not share the same phase-center and overall more space is occupied. The TRX front-end and MMIC feature two RX-Channel for angle of arrival (AoA) measurements. In this publication, results with a single channel back-end as described in [17] for a *D*-Band radar are presented. Other radar systems using this back-end and similar system architecture at 80 GHz [18], [19], 94 GHz [20], and 240 GHz [21], [22] center frequency are presented. The back-end contains the radar control features and power supply, such as the microcontroller ($\mu$C), universal serial bus (USB) interface, direct current (dc)–dc converters, low-dropout (LDO) regulators, low phase noise (PN) reference oscillator (VCXO) for the $\mu$C and the phase-locked loops (PLLs), anti-aliasing filters with variable gain amplifiers, and analog-to-digital converters (ADCs) for IF-signal sampling. With small changes in power supply and firmware, a 3.3-V single PLL-circuit and MMIC combination as in contrast to our previous published systems with a dual PLL-architecture and 5 V can be supported by the back-end.

### A. Transceiver MMIC

The key component of the TRX is the harmonic radar MMIC with its block diagram given in Fig. 6. For the signal synthesis at the fundamental, a VCO is integrated with its output signal split into the TX path over a power amplifier (PA) and the harmonic LO path with a frequency doubler. The frequency-doubled LO path is additionally split and coupled into two direct down-conversion mixers to realize two separate receive channels. For the implementation of the TRX and tag MMIC's, the automotive-qualified production technology B11HFC by Infineon Technologies AG was used, which is

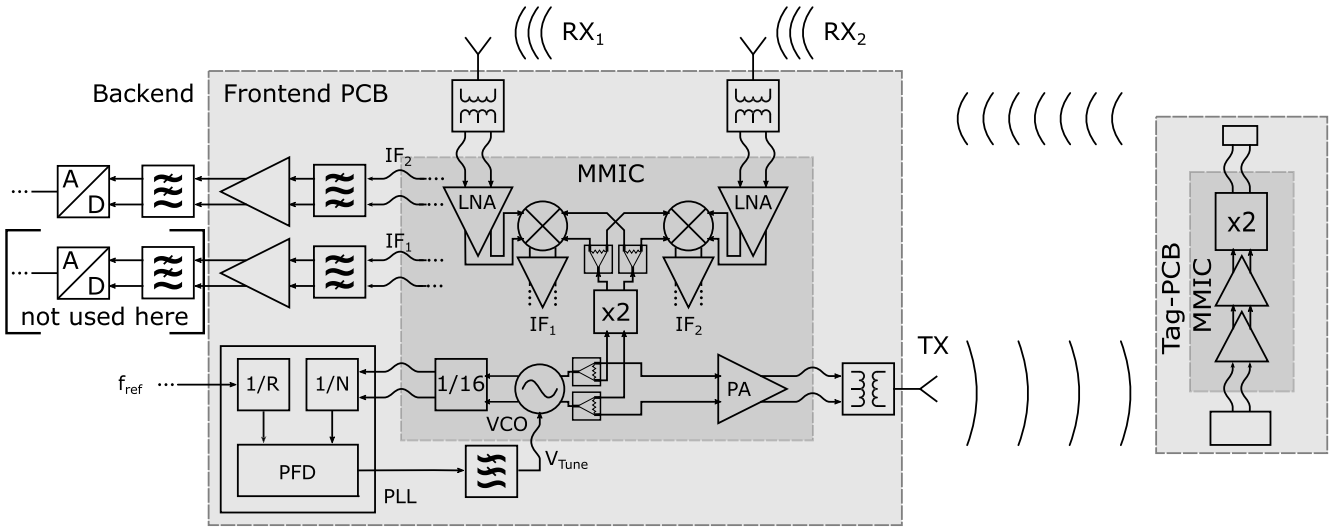


Fig. 6. Simplified schematic of transceiver analog front end including harmonic radar MMIC with one transmitting and two receiving channels and a single nonlinear tag with active frequency doubler MMIC and patch antennas.

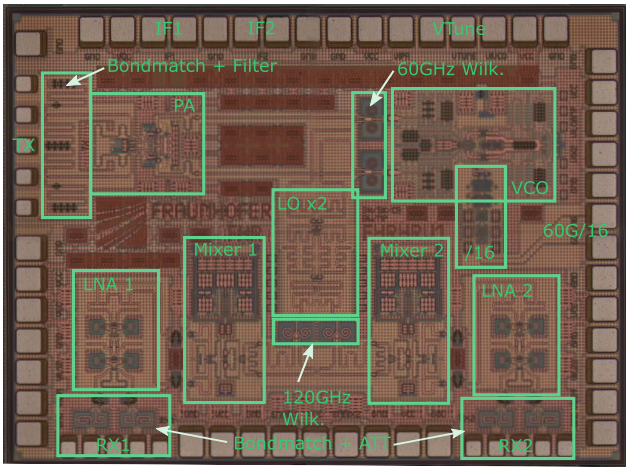


Fig. 7. Micrograph of transceiver MMIC for multiple input, single output (MISO) harmonic Radar (total die size: 1964 × 1448 $\mu$m$^2$).

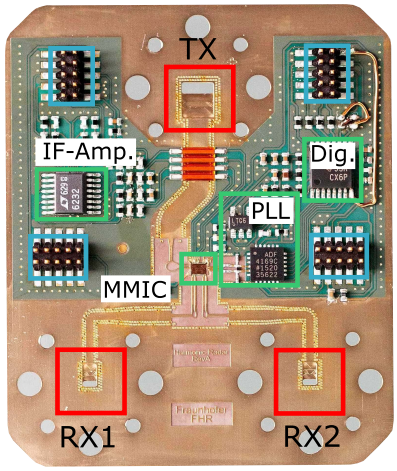


Fig. 8. Photograph of realized harmonic radar front-end (total dimension of 46 × 55 mm$^2$). Marked in red is the waveguide interface to the antennas and in blue the four connectors for the back-end which is not included in this picture.

a 130-nm-BiCMOS SiGe:C technology with an $f_T/f_{\max}$ of 250/370 GHz [23], respectively.

In Fig. 7 a micrograph of the TRX-MMIC is shown. The MMIC's signal-routing and circuit blocks are fully differential to suppress the generation of the second harmonic at the output. The MMIC integrates a VCO, which is tunable from 55 to 67 GHz, and a static divide-by-16 chain for stabilization in a PLL with commercial PLL-circuits. The fundamental output signal of the VCO is distributed by compact lumped element Wilkinson dividers to a PA for the TX signal and the frequency doubler for harmonic LO-path generation. The circuit design of the components at the fundamental frequency is based on the results presented in [13]. The frequency doubler in the LO-path is based on a bootstrapped Gilbert cell frequency doubler similar to [24] which also has a preamplification stage included. The Wilkinson divider network at the second harmonic frequency is splitting the signal equally to each LO-input of the two RX-mixers. The RX channels also include a low noise amplifier (LNA) each for increased sensitivity and gain. Additionally, their reverse isolation decrease the harmonic signal transmitted at the RX. This reduces the necessity of a high LO-to-RX isolation of the mixer since insufficient isolation and a second harmonic signal transmitted from the RX channels results in unwanted detection of linear targets as shown in Fig. 4. For the receiving mixer, a redesign of a full Gilbert cell as presented in [25] was used.

All mm-wave MMIC-to-PCB interfaces include compensation networks for the bond wires and pads at their respective frequency, which also provide ac-coupling for the RF signals and an ESD-path to ground. In the TX-bond wire matching network additionally, a band-stop filter at the harmonic frequency is included which is realized as a shorted quarter wavelength stub at 61 GHz which acts as an open at 61 GHz and as a short at 122 GHz. The MMIC consumes a total of 200 mA at a 3.3-V supply.

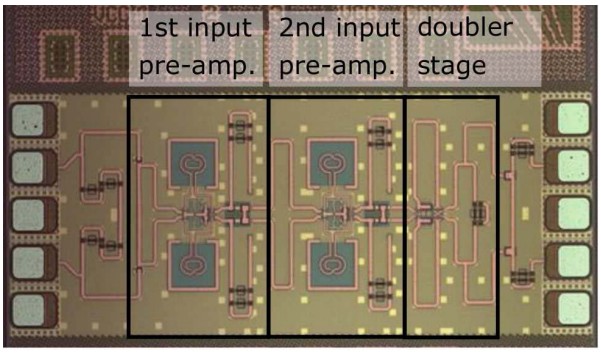


Fig. 9. Micrograph from [16] of MMIC with two pre-amplifiers and bootstrapped Gilbert cell frequency doubler (total die size: 930 × 930 $\mu$m$^2$).

### *B. Transceiver Front-End PCB*

Besides the harmonic Radar MMIC, the front-end includes the PLL circuit for the radar MMIC's VCO which also includes an active loop filter. For ramp generation, the ADF4169 fractional-N frequency synthesizer with a reference frequency at 100 MHz coming from the ultralow noise CVSS-945 reference crystal oscillator on the back-end is used. It features different modulation patterns including triangular modulation for range and velocity determination. The loop filter is designed as an active filter of fourth order with a LT6202 ultralow noise operational amplifier (Op-Amp). The two fully differential received IF-signals of both RX-channels are amplified and bandpass filtered on the front-end PCB by a design based on a LT6232 quad-channel Op-Amp and transmitted to the back-end. In order to be compatible with the existing back-end, a bi-directional level-shifter TXB0106 is also included for the digital PLL-interface. The complete radar system is powered by a single USB 3.0 port and is consuming 710 mA at 5 V.

The front-end has been fabricated on a Rogers RT/duroid 5880 substrate with $\epsilon_r = 2.20$ and $\tan\delta = 0.0009$ at 10 GHz, rolled copper as top-layer metal and copper thick metal cladding with 1 mm thickness on the bottom side. The die can be placed inside an open cavity lasered from the topside on the 1 mm thick copper plane for sufficient heat transfer. The routing of the mm-wave signals is done with highly optimized wideband structures with an additional focus on low loss, feasibility, low cost, and versatility. The realized front-end is shown in Fig. 8. For maximum flexibility, the standardized WR-15 flange is used as a TX interface and two WR-6.5 flanges at the RX interfaces. These are directly milled into the thick metal cladding of the PCB [26] and fed by substrate integrated waveguide (SIW). The SIWs are connected to the MMIC by $\lambda/2$-Baluns and a SIW-to-microstrip coupler. Especially at the RX, the waveguide is valuable because of its lower cutoff at 90 GHz which is blocking the fundamental frequency from direct coupling from TX- to RX-antenna into the RX mixer.

### *C. Active mm-Wave Tag*

The circuit is designed as two cascaded differential cascode amplifiers for improved high-frequency performance.

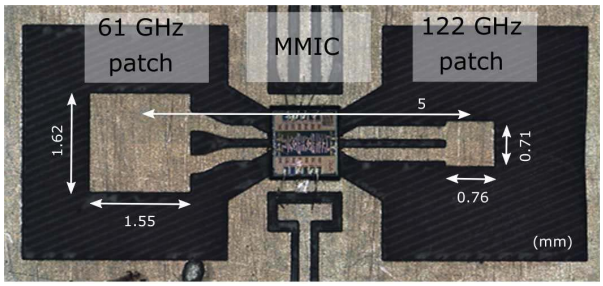


Fig. 10. Picture from [16] of tag consisting of MMIC mounted in an open cavity of PCB connected to TX and RX antenna as differential patch antennas (size of cutout: 10 × 5 mm$^2$).

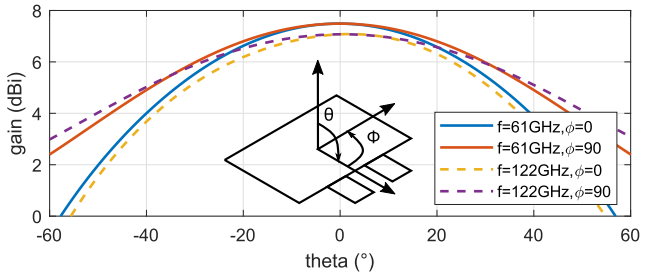


Fig. 11. Simulated gain of differential fed patch antennas as shown in Fig. 10.

Between the common-emitter and common-base stage, a series inductance is used for increased voltage gain. The interstage matching, which is based on transmission lines and a capacitive voltage divider is tuned slightly different for staggered resonances and increased bandwidth. They provide sufficient voltage gain to the weak input signal for more efficient frequency doubling within the desired frequency band. The circuit design is based on the results presented in [24] and the doubler is realized as a bootstrapped Gilbert cell frequency doubler at the output (see Fig. 9). The input and output matching networks are transmission line based and are designed considering the results of a full-wave EM simulation of differential 200-$\mu$m bond wires and the pads. A fully differential design is used for fundamental suppression at the output of the doubler which can otherwise result in stability problems for insufficient output to input isolation. Additionally, the virtual ground increases gain and common-mode rejection ratio. Additional pads besides those for ground and the 3.3-V supply can be used for fine-tuning core currents of the individual stages. The total circuit consumes 40 mA at 3.3 V.

In Fig. 10 a cutout of the Tag-PCB is shown. It is also fabricated on a Rogers RT/duroid 5880 substrate with thick metal cladding. The total size is (10 x 5 mm$^2$ with an antenna-pitch of 5 mm). Both the RX and TX antennas are designed as differential fed patch antennas for a differential PCB-to-MMIC interface without the need of additional baluns and to maintain the fully differential design. They are matched to 100 Ω at 61 and 122 GHz, respectively. In the simulation, the metal surrounding the patch is also included. The results are shown in Fig. 11. The simulated gain is 7.5 dBi for 61 GHz and 7.1 dBi for 122 GHz. They feature a wide linear polarized

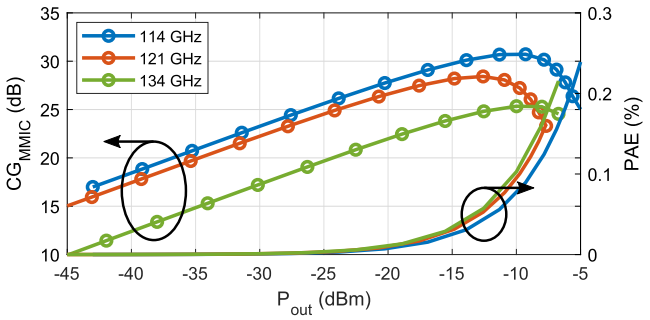


Fig. 12. On-wafer measurement of conversion gain and PAE of MMIC versus output frequency and output power. The maximum conversion gain is 31.3 dB at 115.5-GHz and an input power of −41 dBm..

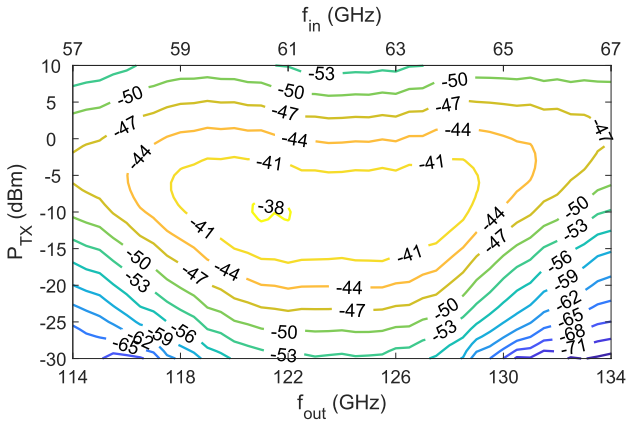


Fig. 13. Free-space conversion gain from [16] of tag versus frequency and output power with the transmitter at 35-cm distance. Maximum conversion gain of −38 dB at 60.75 GHz and −10-dBm transmitter output power.

half-power beamwidth (HPBW) of more than 75° for both frequencies in azimuth and elevation, respectively.

## IV. Measurement Results

### A. CW-Response of Tag With Laboratory Equipment

Several measurements with laboratory equipment were carried out to investigate the tag performance separately. Consider Fig. 12 which shows the conversion gain of the MMIC measured directly at the RF pads in an on-wafer setup. A Keysight PSG is used as an input source for the characterization. The output is measured with a $D$-Band harmonic mixer and spectrum analyzer to handle the small output signal. All adapters and cables are de-embedded from the measurement results. The measurements show that the MMIC has a peak conversion gain of 31.1 dB for an input power of −41 dBm within the measured frequency range. In contrast to the design frequency of 61 and 122 GHz, respectively, the center frequency is shifted to lower frequencies. This is reasonable when considering that bond wire compensation networks are included at the input and output respectively but not present in the measurement. The optimum input power for maximum conversion gain ranges from −41 to −33 dBm. The saturated output power ranges from −6 to −4 dBm at the harmonic frequency. The power-added efficiency (PAE) was not the main concern during the design of this circuit and as a result low since all stages are biased in the linear region for higher gain.

The same measurement equipment was used for conversion gain measurements in a free-space environment with the MMIC mounted on the PCB. Instead of probes, standard gain horns for $V$-Band (WR-15 conical horn, 21 dBi at 61 GHz) and $D$-Band (WR-6 pyramidal horn, 22.2 dBi at 122 GHz) were placed in 35-cm distance to the tag. The results are shown in Fig. 13. One can see that the narrow band patch antennas in conjunction with the bond wires considered in the MMIC design shift the region of maximum conversion gain toward 61 and 122 GHz, respectively. The maximum conversion gain is −38 dB at 60.75 GHz input frequency with 8 GHz bandwidth at −10-dBm transmitter output power with respect to the output frequency at the second harmonic. The FSPL for this configuration is 30.5 dB considering 7.5-dBi gain for the 61-GHz patch antenna. The maximum-gain measurement matches well to the on-wafer results. At an input power of −41.5 dBm the on-wafer measurements resulted in a conversion gain of 28.5 dB at 61 GHz which results in an input power of −13 dBm at the 122-GHz patch. Including the FSPL of 35.5 dB for the return path of the transmission at the harmonic frequency, the expected power is −48.5 dBm or −38-dB conversion gain, respectively. The total logarithmic free-space gain $\mathrm{CG}_{\text{free-space}}$ transfer function is

$$\mathrm{CG}_{\text{free-space}} = P_{\mathrm{RX}} - P_{\mathrm{TX}} = -\mathrm{FSPL}_{61} + \mathrm{CG}_{\mathrm{MMIC}} - \mathrm{FSPL}_{122}. \tag{9}$$

### B. FMCW-Response of Tag With Harmonic Radar TRX

In this section, the entire system by evaluation of the sampled IF-signal is described. For this purpose, the tag is mounted on a metallic fixture with polarization and orientation matched for tag and TRX. Even though the TRX is able to modulate over a wider frequency range the modulation bandwidth is set to 4 GHz (60–64 GHz) which corresponds to the bandwidth of the tag. The average measured output power within this range is 6 dBm at the $V$-Band antenna flange of the TRX. The ramp duration is set to 4 ms and a saw-tooth modulation with 1-ms recovery time is chosen. For this measurement the standard gain horns for $V$- and $D$-band are used again.

In Fig. 14 the time-domain signal of the tag positioned 1 m in front of the TRX is shown. The sampled data show a signal with a fairly constant amplitude which is superimposed by low-frequency components especially from 60 to 62 GHz. They result from nonideal isolation between TX and RX on the MMIC, PCB, and between the antennas. This becomes evident when looking at the frequency-domain representation of this signal (see. Fig.15). The results show a strong response at the expected distance. The −6 dB-width in this uncalibrated measurement setup is 4 cm which corresponds to an effective bandwidth of 7.5 GHz or 187 % with respect to the sweep at the fundamental frequency. Additionally, the low-frequency components which correspond to a distance below 0.25 m are observed. Above 1-m distance, multiple false targets around 40 dB lower are observed which results from multipath

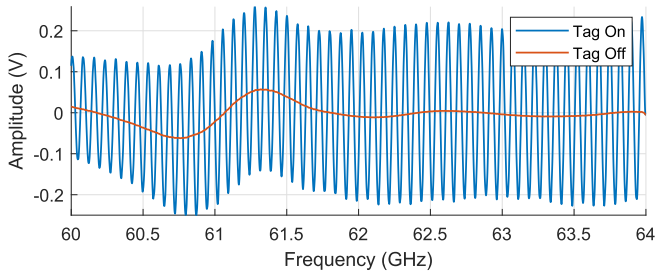


Fig. 14. Time-domain representation of uncalibrated IF-signal with single tag switched on and off in 1-m distance for a down-chirp of 4-GHz bandwidth in 4 ms.

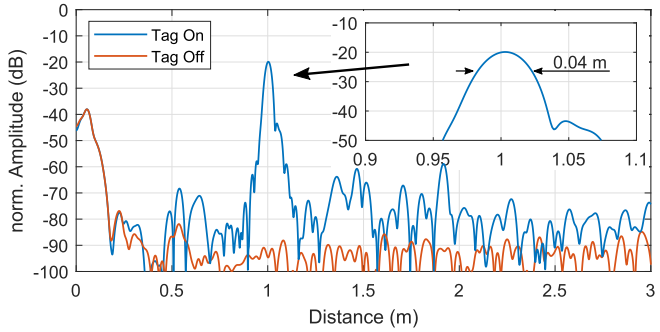


Fig. 15. Frequency-domain representation of uncalibrated IF-signal with single tag switched on and off in 1-m distance for a down-chirp of 4-GHz bandwidth in 4 ms and magnification of the target's peak. For decreased sidelobe level, a Hann window is applied.

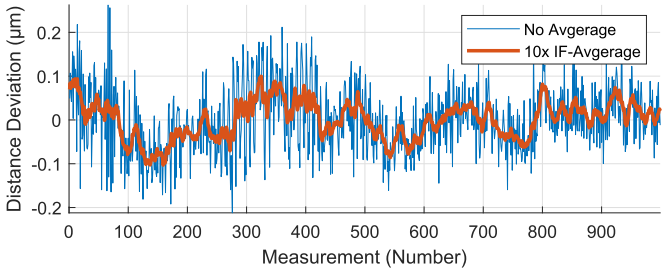


Fig. 16. Stability of the system is demonstrated by 1000 measurements to the same target at 1-m distance. The standard deviation of this set of measurements is 0.074 $\mu$m or 0.022° phase jitter.

propagation within the return path due to the wide HPBW of the patch antennas on the tag. With the tag turned off only a weak linear response (60 dB lower) of the fixture at 0.5 m becomes visible. At 1-m distance, the SNR is 70 dB and no linear reflection at the second harmonic from the fixture is detected.

For high precision radar, the long-term stability is an important figure of merit. For this purpose, 1000 consecutive measurements with a pulse repetition frequency of 100 Hz are performed. Consider Fig. 16 which shows the measured distance jitter. The distance deviation lies within a 0.47-$\mu$m range. The standard deviation of this set of measurements is 0.074 $\mu$m which corresponds to 0.022° phase deviation at the RX center frequency. With an averaging over 10 measurements, the jitter can be improved to 0.042 $\mu$m and 0.016°, respectively.

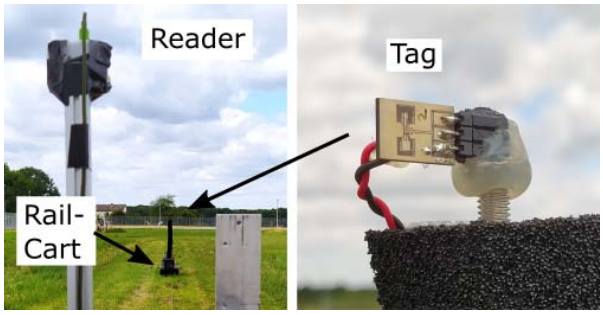


Fig. 17. Measurement setup for outdoor range measurements on a linear track. The scenario as seen from the reader with rail-cart moving in front (left) and a detailed look at the tag which is mounted on the rail cart (right).

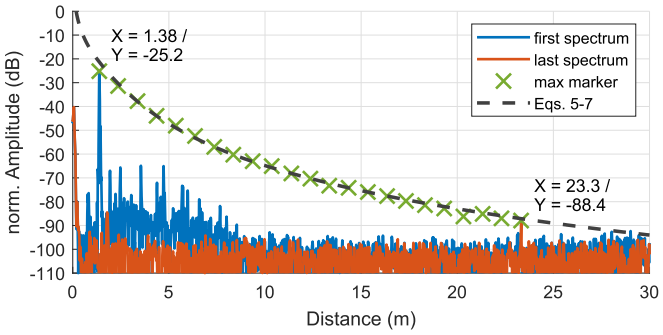


Fig. 18. Superposition of spectra from a measurement setup with the tag moving along a linear track in the range from 1.38 to 23.3 m. Shown are the results in the beginning and end of the track. The amplitude at each point follows the analytically derived level.

With identical settings, a measurement on a linear track (cp. Fig. 17) in the range of around 1 to 23 m with 1-m distance between each position is carried out. In Fig. 18 the spectra of the measurements in the beginning (1.38 m) and end (23.3 m) of the linear track are shown. Also included in the graph is a marker representing each maximum of the measurement points in between. The amplitude derived analytically from Eqs. 5-7 which is calculated with results from previous measurements (dashed line) matches well. With 6-dBm output power, which is measured at the $V$-Band waveguide flange and a total FSPL of 40 dB at 61 GHz and 1-m distance, the tag MMIC is excited in the saturated region. At around 5 m the tag MMIC is in the quadratic region which means that above this distance the power transfer function follows the $1/R^6$-dependence. At 23.3 m the FSPL is 67.4 dB at 61 GHz and 71.8 dB at 122 GHz. The normalized amplitude is $-88.4$ dB and only close above the noise floor of the system. The measurements also show that for the increased distance the range resolution decreases from 4 cm at 1-m distance to 8.86 cm (corresponds to 3.34 GHz) at 23.3-m distance. This becomes evident when considering the results in Fig. 13 which shows that the bandwidth of the tag is decreasing with lower input power.

## V. Conclusion

In this article, we presented a highly integrated 61-/122-GHz harmonic radar system based on an active frequency doubler tag in a 130-nm-BiCMOS SiGe:C technology. So far, most

systems presented in the literature are below the mm-wave range where higher output power and receiver sensitivity, as well as lower FSPL, benefit the overall detection capabilities and it is concluded that harmonic radar in the mm-wave region is inefficient. However, measurements have shown that with modern RF semiconductor technology the high FSPL can be overcome by designing active tags with sufficient conversion gain. In on-wafer measurements, the MMIC has a power conversion gain of 31 dB for −41-dBm input power. In a free-space measurement with the quasi monostatic harmonic FMCW radar TRX, a strong reflection at 1-m distance with an amplitude 70 dB over the receiver sensitivity threshold is observed. The range resolution including a Hann window function is 4 cm for a frequency sweep of 4 GHz at the fundamental. The active tag is still detectable at a range of 23 m. However with stronger focusing antennas, especially on the tag, the range can be improved even more. The results look promising to use these tags in short-range applications with no power constraint.

To the best of the authors' knowledge, this is the first time that a harmonic radar system with active tags in the mm-wave range are published to overcome the high FSPL and heavily extend the range. The push toward higher frequencies which is correlated with higher bandwidth, resolution, accuracy, and compactness can enable many more applications. The system presented here is a step toward highly integrated and compact harmonic radar use in applications beyond tracking insects, for example, in the industrial or medical area where small reflectors need to be detected uniquely and precise with high robustness to clutter.

## ACKNOWLEDGMENT

The authors would also like to thank Infineon Technologies AG and its Staff for the fabrication of the MMIC and Simon Küppers from 2pi-Labs for the fruitful discussions regarding circuit design in the *D*-Band.

## REFERENCES

[1] L. Piotrowsky, T. Jaeschke, S. Kueppers, J. Siska, and N. Pohl, "Enabling high accuracy distance measurements with FMCW radar sensors," *IEEE Trans. Microw. Theory Techn.*, vol. 67, no. 12, pp. 5360–5371, Dec. 2019.

[2] G. Storz and A. Lavrenko, "Compact low-cost FMCW harmonic radar for short range insect tracking," in *Proc. IEEE Int. Radar Conf. (RADAR)*, Apr. 2020, pp. 642–647.

[3] H. M. Aumann and N. W. Emanetoglu, "A wideband harmonic radar for tracking small wood frogs," in *Proc. IEEE Radar Conf.*, May 2014, pp. 0108–0111.

[4] D. Psychoudakis, W. Moulder, C.-C. Chen, H. Zhu, and J. L. Volakis, "A portable low-power harmonic radar system and conformal tag for insect tracking," *IEEE Antennas Wireless Propag. Lett.*, vol. 7, pp. 444–447, 2008.

[5] S. Bottigliero, D. Milanesio, M. Saccani, R. Maggiora, A. Viscardi, and M. M. Gallesi, "An innovative harmonic radar prototype for miniaturized lightweight passive tags tracking," in *Proc. IEEE Radar Conf. (RadarConf)*, Apr. 2019, pp. 1–6.

[6] Z.-M. Tsai *et al.*, "A high-range-accuracy and high-sensitivity harmonic radar using pulse pseudorandom code for bee searching," *IEEE Trans. Microw. Theory Techn.*, vol. 61, no. 1, pp. 666–675, Jan. 2013.

[7] Y.-T. Liu, M.-L. Hsu, H. Wang, and Z.-M. Tsai, "A differential miniature transponder for 9.4/18.8 GHz harmonic bee searching radar with low gain degradation from bee's body," in *IEEE MTT-S Int. Microw. Symp. Dig.*, May 2016, pp. 1–4.

[8] B. G. Colpitts and G. Boiteau, "Harmonic radar transceiver design: Miniature tags for insect tracking," *IEEE Trans. Antennas Propag.*, vol. 52, no. 11, pp. 2825–2832, Nov. 2004.

[9] N. Tahir and G. Brooker, "The investigation of millimetre wave optical harmonic transponders and radar for monitoring small insects," in *Proc. IEEE Topical Conf. Wireless Sensors Sensor Netw. (WiSNet)*, Jan. 2013, pp. 22–24.

[10] V. Viikari *et al.*, "Technical solutions for automotive intermodulation radar for detecting vulnerable road users," in *Proc. VTC Spring-IEEE 69th Veh. Technol. Conf.*, Apr. 2009, pp. 1–5.

[11] L. Goertschacher and J. Grosinger, "Localization of signal pattern based UHF RFID sensor tags," *IEEE Microw. Wireless Compon. Lett.*, vol. 29, no. 11, pp. 753–756, Nov. 2019.

[12] C. M. Schmid, R. Feger, and A. Stelzer, "Millimeter-wave phase-modulated backscatter transponder for FMCW radar applications," in *IEEE MTT-S Int. Microw. Symp. Dig.*, Jun. 2011, pp. 1–4.

[13] C. Bredendiek *et al.*, "A 61-GHz SiGe transceiver frontend for energy and data transmission of passive RFID single-chip tags with integrated antennas," *IEEE J. Solid-State Circuits*, vol. 53, no. 9, pp. 2441–2453, Sep. 2018.

[14] M. Vossiek and P. Gulden, "The switched injection-locked oscillator: A novel versatile concept for wireless transponder and localization systems," *IEEE Trans. Microw. Theory Techn.*, vol. 56, no. 4, pp. 859–866, Apr. 2008.

[15] A. Strobel, C. Carlowitz, R. Wolf, F. Ellinger, and M. Vossiek, "A millimeter-wave low-power active backscatter tag for FMCW radar systems," *IEEE Trans. Microw. Theory Techn.*, vol. 61, no. 5, pp. 1964–1972, May 2013.

[16] S. Hansen, C. Bredendiek, and N. Pohl, "Active reflector tag for millimeter wave harmonic radar at 61/122 GHz ism band based on 130 nm-BICMOS SiGe: C technology," in *IEEE MTT-S Int. Microw. Symp. Dig.*, 2020, pp. 611–614.

[17] T. Jaeschke, C. Bredendiek, S. Kuppers, and N. Pohl, "High-precision D-band FMCW-radar sensor based on a wideband SiGe-transceiver MMIC," *IEEE Trans. Microw. Theory Techn.*, vol. 62, no. 12, pp. 3582–3597, Dec. 2014.

[18] N. Pohl, T. Jaeschke, and K. Aufinger, "An ultra-wideband 80 GHz FMCW radar system using a SiGe bipolar transceiver chip stabilized by a fractional-N PLL synthesizer," *IEEE Trans. Microw. Theory Techn.*, vol. 60, no. 3, pp. 757–765, Mar. 2012.

[19] N. Pohl, T. Jaeschke, S. Kuppers, C. Bredendiek, and D. Nusler, "A compact ultra-wideband mmWave radar sensor at 80 GHz based on a SiGe transceiver chip (focused session on highly-integrated millimeter-wave radar sensors in SiGe BiCMOS technologies)," in *Proc. 22nd Int. Microw. Radar Conf. (MIKON)*, May 2018, pp. 345–347.

[20] B. Welp *et al.*, "Versatile dual-receiver 94-GHz FMCW radar system with high output power and 26-GHz tuning range for high distance applications," *IEEE Trans. Microw. Theory Techn.*, vol. 68, no. 3, pp. 1195–1211, Mar. 2020.

[21] S. Thomas, C. Bredendiek, and N. Pohl, "A SiGe-based 240-GHz FMCW radar system for high-resolution measurements," *IEEE Trans. Microw. Theory Techn.*, vol. 67, no. 11, pp. 4599–4609, Nov. 2019.

[22] S. Thomas, C. Bredendiek, T. Jaeschke, F. Vogelsang, and N. Pohl, "A compact, energy-efficient 240 GHz FMCW radar sensor with high modulation bandwidth," in *Proc. German Microw. Conf. (GeMiC)*, Mar. 2016, pp. 397–400.

[23] J. Bock *et al.*, "SiGe HBT and BiCMOS process integration optimization within the DOTSEVEN project," in *Proc. IEEE Bipolar/BiCMOS Circuits Technol. Meeting (BCTM)*, Oct. 2015, pp. 121–124.

[24] S. Kueppers, K. Aufinger, and N. Pohl, "A fully differential 100–140 GHz frequency quadrupler in a 130 nm SiGe: C technology for MIMO radar applications using the bootstrapped Gilbert-cell doubler topology," in *Proc. IEEE 17th Topical Meeting Silicon Monolithic Integr. Circuits RF Syst. (SiRF)*, Jan. 2017, pp. 37–39.

[25] C. Bredendiek, N. Pohl, T. Jaeschke, K. Aufinger, and A. Bilgic, "A highly-linear low-power down-conversion mixer for monostatic broadband 80 GHz FMCW-radar transceivers," in *Proc. Prog. Electromagn. Res. Symp. (PIERS)*, Kuala Lumpur, Malaysia, Mar. 2012, pp. 333–337.

[26] S. Hansen and N. Pohl, "A W-band stepped impedance transformer transition from SIW to RWG for thin single layer substrates with thick metal cladding," in *Proc. 49th Eur. Microw. Conf. (EuMC)*, Oct. 2019, pp. 352–355.

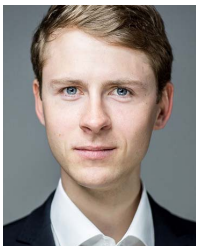

**Steffen Hansen** (Graduate Student Member, IEEE) received the B.Sc. and M.Sc. degrees in electrical engineering from the Hamburg University of Technology, Hamburg, Germany, in 2014 and 2017, respectively.

Since 2016, he has been with the Department of Integrated Circuits and Sensor Systems, Fraunhofer Institute for High Frequency Physics and Radar Techniques, Wachtberg, Germany. His current research activities are in the field of integrated SiGe circuits for mm-wave harmonic radar systems. He is also involved in FMCW radar designs from 50 to 180 GHz.

Mr. Hansen is a member of EUMA.

**Christian Bredendiek** (Member, IEEE) was born in Gelsenkirchen, Germany, in 1981. He received the Dipl.Ing. and Dr.Ing. degrees in electrical engineering from Ruhr University Bochum, Bochum, Germany, in 2008 and 2014, respectively.

From 2008 to 2014, he was a Research Assistant with the Institute of Integrated Systems, Ruhr University Bochum. Since 2015, he has been with the Department of Integrated Circuits and Sensor Systems, Fraunhofer Institute for High Frequency Physics and Radar Techniques, Wachtberg, Germany. His current research interests include frequency synthesis, working on system concepts and integrated circuits for various mm-wave applications.

Dr. Bredendiek was a recipient of the EuMIC Best Paper Award from European Microwave Week in 2012.

**Gunnar Briese** received the Dipl.Ing. (FH) degree in mechatronics from the FH Aachen—University of Applied Sciences, Aachen, Germany, in 2007.

Since 2007, he has been with the Department of Integrated Circuits and Sensor Systems, Fraunhofer Institute for High Frequency Physics and Radar Techniques, Wachtberg, Germany. His current research interests focus on radar-based altimeters and collision avoidance radars for UAV usage.

**Nils Pohl** (Senior Member, IEEE) received the Dipl.-Ing. and Dr.Ing. degrees in electrical engineering from Ruhr University Bochum, Bochum, Germany, in 2005 and 2010, respectively.

From 2006 to 2011, he was a Research Assistant with Ruhr University Bochum, where he was involved in integrated circuits for millimeter-wave (mm-wave) radar applications. In 2011, he became an Assistant Professor with Ruhr University Bochum. In 2013, he became the Head of the Department of mm-wave Radar and high frequency sensors with the Fraunhofer Institute for High Frequency Physics and Radar Techniques, Wachtberg, Germany. In 2016, he became a Full Professor for Integrated Systems with Ruhr University Bochum. He has authored or coauthored more than 100 scientific articles and has issued several patents. His current research interests include ultra-wideband mm-wave radar, design, and optimization of mm-wave integrated SiGe circuits and system concepts with frequencies up to 300 GHz and above, as well as frequency synthesis and antennas.

Dr. Pohl is a member of VDE, ITG, EUMA, and URSI. He was a co-recipient of the 2009 EEEfCom Innovation Award, the 2012 EuMIC Prize, and the 2015 Best Demo Award of the IEEE Radio Wireless Week, and a recipient of the Karl-Arnold Award of the North Rhine-Westphalian Academy of Sciences, Humanities and the Arts in 2013 and the IEEE MTT Outstanding Young Engineer Award in 2018.